The transverse field Richtmyer-Meshkov instability in magnetohydrodynamics

V. Wheatley, R. Samtaney, D. I. Pullin, and R. M. Gehre

Citation: Physics of Fluids (1994-present) **26**, 016102 (2014); doi: 10.1063/1.4851255
View online: http://dx.doi.org/10.1063/1.4851255
View Table of Contents: http://scitation.aip.org/content/aip/journal/pof2/26/1?ver=pdfcov
Published by the AIP Publishing

PHYSICS OF FLUIDS **26**, 016102 (2014)

The transverse field Richtmyer-Meshkov instability in magnetohydrodynamics

V. Wheatley,[1] R. Samtaney,[2] D. I. Pullin,[3] and R. M. Gehre[1]
[1]*School of Mechanical and Mining Engineering, University of Queensland, Queensland 4072, Australia*
[2]*Mechanical Engineering, King Abdullah University of Science and Technology, Thuwal 23955-6900, Saudi Arabia*
[3]*Graduate Aerospace Laboratories, California Institute of Technology, Pasadena, California 91125, USA*

(Received 2 July 2013; accepted 26 November 2013; published online 10 January 2014)

The magnetohydrodynamic Richtmyer-Meshkov instability is investigated for the case where the initial magnetic field is unperturbed and aligned with the mean interface location. For this initial condition, the magnetic field lines penetrate the perturbed density interface, forbidding a tangential velocity jump and therefore the presence of a vortex sheet. Through simulation, we find that the vorticity distribution present on the interface immediately after the shock acceleration breaks up into waves traveling parallel and anti-parallel to the magnetic field, which transport the vorticity. The interference of these waves as they propagate causes the perturbation amplitude of the interface to oscillate in time. This interface behavior is accurately predicted over a broad range of parameters by an incompressible linearized model derived presently by solving the corresponding impulse driven, linearized initial value problem. Our use of an equilibrium initial condition results in interface motion produced solely by the impulsive acceleration. Nonlinear compressible simulations are used to investigate the behavior of the transverse field magnetohydrodynamic Richtmyer-Meshkov instability, and the performance of the incompressible model, over a range of shock strengths, magnetic field strengths, perturbation amplitudes and Atwood numbers. [http://dx.doi.org/10.1063/1.4851255]

I. INTRODUCTION

When a perturbed interface separating fluids with different densities is impulsively accelerated, typically by a shock wave, the interface becomes unstable and the perturbations grow. This scenario was first considered by Markstein.[1] A rigorous theoretical and numerical analysis of the flow was later presented by Richtmyer,[2] whose predictions were confirmed by the shock tube experiments of Meshkov.[3] This instability is, therefore, known as the Richtmyer-Meshkov instability (RMI). The canonical situation in which the RMI occurs is shown in Fig. 1(a), where a shock wave interacts with a sinusoidal density interface. Figure 1(b) shows the effect of the instability on the interface after the interaction is complete: it has become highly distorted which can lead to significant mixing between the two fluids.

The RMI is important in a wide variety of applications. One of the most significant of these is inertial confinement fusion (ICF), which has been a major impetus for the study of shock accelerated interfaces.[4] In current ICF experiments, rapid ablation of a spherical capsule drives an implosion into the deuterium-tritium fuel contained within.[5] The RMI promotes mixing between the capsule material and the fuel. This mixing limits the final compression of the fuel and hence the possibility of achieving energy break-even or production.[6] The RMI is also important in astrophysical phenomena. It has been used to account for the lack of stratification in the products of supernova 1987A and is required in stellar evolution models.[7] In supersonic and hypersonic air breathing engines, the RMI may be used to enhance the mixing of fuel and air.[8] The RMI also arises in many combustion

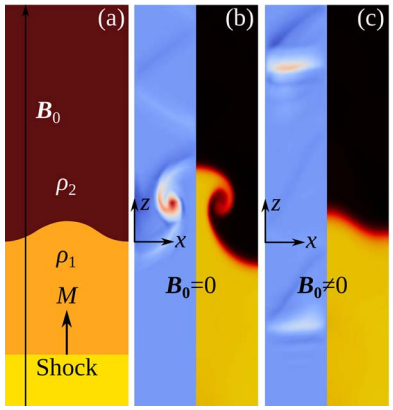

FIG. 1. (a) Initial condition for the normal field MHD RMI simulations of Wheatley *et al.*[15] (b) Post shock-interaction vorticity ($\nabla \times \mathbf{u}$, left half frames) and density (ρ, right half frames) fields for an incident shock sonic Mach number of $M = 2$, a density ratio of $\rho_2/\rho_1 = 1/3$, and a ratio of specific heats of $\gamma = 5/3$ when no magnetic field is present. (c) Post shock-interaction vorticity and density fields for the same case as (b) when an initial magnetic field of non-dimensional strength $\beta^{-1} = B^2/2p_0 = 1/16$ is present, where p_0 is the initial thermodynamic pressure

systems where shock-flame interactions occur; the resulting instability is significant in deflagration-to-detonation transition.[9] In reflected shock tunnels, the RMI is one mechanism for explaining driver gas contamination.[10]

In the first two applications of the RMI listed above, inertial confinement fusion and astrophysical phenomena, the media involved may be in the plasma state and hence be affected by magnetic fields. It is well known that the linear growth rate of the Rayleigh-Taylor instability, a hydrodynamic instability related to the RMI, is mitigated at high wavenumbers in the presence of a magnetic field.[11] The effect of a magnetic field on the RMI, however, had not been investigated until Samtaney[12] demonstrated, via numerical simulations, that for the magnetic field orientation shown in Fig. 1(a) the growth of the RMI is suppressed. This can clearly be seen by comparing Fig. 1(b), which shows the post-interaction density contours when no magnetic field is present, and Fig. 1(c), which shows the result of an identical simulation carried out in the presence of a magnetic field. It was shown by Wheatley *et al.*[13] that the suppression of the instability is caused by changes in the shock refraction process at the interface with the application of a magnetic field that leaves the interface vorticity free. Subsequently, Wheatley *et al.*[14] carried out an analytical linear analysis of an impulsively accelerated density interface in the presence of a normal magnetic field. This successfully models the behavior of the interface in the magnetohydrodynamic (MHD) RMI for weak shocks and magnetic fields.[15] The other canonical MHD RMI case, where the magnetic field is parallel to the density interface, was linearly modeled by Cao *et al.*[16] However, their formulation, which differs from that used in Wheatley *et al.*,[14] results in oscillation of the interface even when no forcing is present. In addition, their model has not been compared to other results to assess its accuracy and appropriateness. Motivated by understanding magnetic field amplification in supernova remnants, Sano *et al.*[17] have simulated the two-dimensional MHD RMI for three different initial magnetic field orientations: normal, parallel, and at an angle $\pi/4$ to the interface. Their study, however, focused on a very weak initial magnetic field ($\beta = 10^8$) that had little effect on the dynamics of the RMI.[17]

The recent intense interest in the RMI[12,15,16,18–21] is primarily motivated by its significance in inertial confinement fusion, a technology with the potential to demonstrate highly efficient carbon-free energy production.[22] In ICF, suppression of the instability is desirable and we have established that in certain idealized cases, a magnetic field can suppress the MHD RMI. Consequently, investigating the suppression of the RMI by a magnetic field of different orientations is an important research topic. Furthermore, in recent experiments, ICF targets were immersed in a seed magnetic field before implosion with the goal of enhancing compression through electron confinement.[23] This resulted in the observed ion temperature and neutron yield being significantly enhanced, demonstrating that the concept utilizing magnetic fields in ICF experiments has merit. In the present work, we formulate

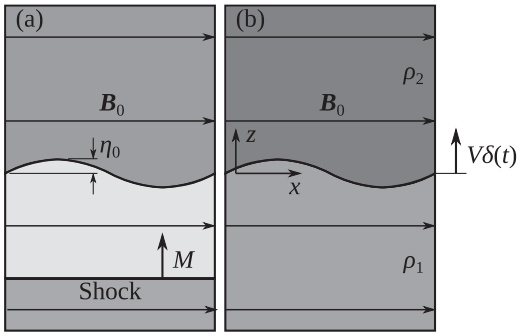

FIG. 2. (a) Initial condition for the shock driven compressible MHD RMI with a transverse magnetic field. (b) Initial condition for the corresponding impulse driven, incompressible model problem.

a linear incompressible model for the MHD RMI when the magnetic field is parallel to the mean interface location, as shown in Fig. 2. The approach of Wheatley *et al.*[14] is used so that interface motion occurs only as a result of the impulsive acceleration and not due to the initial condition. The behavior predicted by this model is then compared to the results of shock driven simulations of the full nonlinear compressible ideal MHD equations. This allows the appropriateness and accuracy of the model to be investigated and reveals new details of the flow physics that were not seen in the work of Cao *et al.*[16] The behavior of the MHD RMI and the performance of the model as problem parameters are altered to increase the nonlinearity of the flow are also documented.

II. INCOMPRESSIBLE MODEL

A. Flow formulation and equations of motion

The initial condition for the problem under consideration is shown in Fig. 2(a): A shock wave of sonic Mach number M is set-up to impact a sinusoidally perturbed density interface in the presence of a transverse magnetic field, $\mathbf{B}$. Here $M = U_S/a$ where U_S is the shock speed and a is the speed of sound. The corresponding incompressible model problem is shown in Fig. 2(b). The shock acceleration of the fluid is replaced by an impulsive acceleration in the z-direction, $V\delta(t)$, where $\delta(t)$ is the Dirac delta function in time and $V \ll c$, the speed of light. This accelerates uniform quiescent conducting fluids of densities ρ_1 and ρ_2, respectively, separated by an interface with initial perturbation amplitude η_0 and wavelength λ. The initial magnetic field, $\mathbf{B}_0 = B\hat{\mathbf{e}}_x$, is aligned with the mean interface location in the x-direction and has non-dimensional strength $\beta^{-1} = B^2/(2\mu_0 p_0)$, where p_0 is the uniform initial pressure and μ_0 is the permeability of vacuum.

The ideal MHD variables are non-dimensionalized using a reference density ρ_0, pressure p_0, and length scale L. The non-dimensional variables are given by

$$\hat{\mathbf{x}} = \frac{\mathbf{x}}{L}, \hat{t} = \frac{t}{L/\sqrt{p_0/\rho_0}}, \hat{\rho} = \frac{\rho}{\rho_0}, \hat{p} = \frac{p}{p_0}, \hat{\mathbf{u}} = \frac{\mathbf{u}}{\sqrt{p_0/\rho_0}}, \hat{\mathbf{B}} = \frac{\mathbf{B}}{\sqrt{\mu_0 p_0}},$$

where $\mathbf{x} \equiv (x, y, z)^T$, $\mathbf{u} \equiv (u, v, w)^T$ is velocity and $\mathbf{B} \equiv (B_x, B_y, B_z)^T$ is the magnetic field. From here on, we consider the problem in non-dimensional form with the carets omitted for clarity. We seek solutions to the model problem that satisfy the linearized equations of ideal, incompressible MHD. The nonlinear equations from which these are derived govern the evolution of an incompressible, quasi-neutral conducting fluid if viscosity, thermal conductivity, the Hall effect, and electrical resistivity are neglected.[25] In the mathematically convenient reference frame with acceleration $V\delta(t)\mathbf{e}_z$ that moves with the interface, these equations are

$$\nabla \cdot \mathbf{u} = 0, \tag{1}$$

$$\rho \frac{\partial \mathbf{u}}{\partial t} + \rho\,(\mathbf{u} \cdot \nabla)\,\mathbf{u} = -\nabla p + (\nabla \times \mathbf{B}) \times \mathbf{B} + \mathbf{f} - \rho V \delta(t)\mathbf{e}_z, \tag{2}$$

$$\nabla \cdot \mathbf{B} = 0, \tag{3}$$

$$\frac{\partial \mathbf{B}}{\partial t} = \nabla \times (\mathbf{u} \times \mathbf{B}). \tag{4}$$

The forcing that impulsively accelerates the fluids is given by

$$\mathbf{f} = [\rho_1 + H(z)(\rho_2 - \rho_1)]\, V\delta(t)\mathbf{e}_z,$$

where $H(z)$ is the Heaviside function. The base-flow about which the governing equations are linearized results from subjecting uniform fluids separated by an unperturbed interface at $z = 0$ to the impulsive body force $\mathbf{f}$. In this case, $\mathbf{f}$ is exactly balanced by the term in Eq. (2) that arises due to the use of an accelerating reference frame. Thus, the base-flow (denoted with a subscript 0) in the chosen frame of reference is identical to the initial conditions and is given by

$$\rho_0(z) = \rho_1 + H(z)\,(\rho_2 - \rho_1)\,, \tag{5}$$

$$u_0 = 0,\ w_0 = 0,\ B_{x0} = B,\ B_{z0} = 0,\ p_0(z,t) = p_0. \tag{6}$$

B. Linearized initial value problem

Imposing an initial perturbation $h(x, t) = \eta(t)e^{ikx} \ll \lambda$ on the interface location produces the required initial condition for the model problem. The linearized equations for the perturbations to the base-flow are then obtained by setting the density equal to

$$\rho(x, z, t) = \rho_1 + H[z - h(x, t)](\rho_2 - \rho_1)$$

and by assuming that all other flow quantities have the form $q(x, z, t) = q_0(z) + q'(x, z, t)$, where q' are small perturbations to the base-flow. Substituting these expressions into Eqs. (1)–(4) and neglecting terms involving products of perturbations yields

$$\frac{\partial u'}{\partial x} + \frac{\partial w'}{\partial z} = 0, \tag{7}$$

$$\rho\frac{\partial u'}{\partial t} + \frac{\partial p'}{\partial x} = 0, \tag{8}$$

$$\rho\frac{\partial w'}{\partial t} + \frac{\partial p'}{\partial z} + B\left(\frac{\partial B_x'}{\partial z} - \frac{\partial B_z'}{\partial x}\right) = (\rho_2 - \rho_1)\,[H(z) - H(z-h)]\,V\delta\,(t)\,, \tag{9}$$

$$\frac{\partial B_x'}{\partial x} + \frac{\partial B_z'}{\partial z} = 0, \tag{10}$$

$$\frac{\partial \mathbf{B}'}{\partial t} - B\frac{\partial \mathbf{u}'}{\partial x} = 0. \tag{11}$$

The forcing of the perturbations due to the impulse at $t = 0^+$ is non-zero only in the vanishingly small region $z \in [0, h(x, t)]$. Our approach is to account for the forcing in the matching conditions between homogeneous solutions that are valid above and below this region. To obtain the homogeneous solutions, we assume that all perturbations have the form $q'(x, z, t) = \hat{q}(z, t)e^{ikx}$ then take the temporal Laplace transforms of Eqs. (7)–(11) outside of the forced region. Initial conditions are taken at $t = 0^-$, when there are no perturbations to the velocity or magnetic field. The resulting transformed homogeneous equations are

$$ikU_j(z, s) + DW_j(z, s) = 0, \tag{12}$$

$$s\rho_j U_j(z, s) = -ikP_j(z, s), \tag{13}$$

$$s\rho_j W(z,s) = -DP_j(z,s) - B\left[DH_x(z,s) - ikH_z(z,s)\right], \tag{14}$$

$$ikH_{x_j}(z,s) + DH_{z_j}(z,s) = 0, \tag{15}$$

$$sH_{x_j}(z,s) = ikBU_j(z,s), \tag{16}$$

$$sH_{z_j}(z,s) = ikBW_j(z,s), \tag{17}$$

where U, W, H_x, H_z, and P are the temporal Laplace transforms of $\hat{u}$, $\hat{w}$, $\hat{B}_x$, $\hat{B}_z$, and $\hat{p}$, respectively, $j = 1$ or 2, s is the Laplace variable and $D \equiv d/dz$. Equations (12)–(17) can then be combined to give a single differential equation for the transformed vertical velocity magnitude in each fluid,

$$D^2 W_j(z,s) - k^2 W_j(z,s) = 0, \tag{18}$$

Eq. (18) has the general solution

$$W_j = A_j(s)\, e^{kz} + B_j(s)\, e^{-kz}. \tag{19}$$

This general solution lacks the wave-like modes of the form $H(t \pm z\sqrt{\rho_j/B_z})f(t \pm z\sqrt{\rho_j/B_z})$ that were present in the normal field case.[14] These modes were responsible for transporting the vorticity generated by impulse away from the interface, which suppressed growth in the amplitude of its perturbations.[15] Thus, the mechanism by which the RMI was suppressed in the normal field case is apparently absent in this model.

C. Matching conditions

The unknown coefficient functions in Eq. (19) must now be determined in each fluid. The requirement that perturbations be bounded as $|z| \to \infty$, assuming $k > 0$, implies that $A_2(s) = 0$ and $B_1(s) = 0$. The transformed velocity magnitudes in each fluid then simplify to

$$W_1(z,s) = A_1(s)\, e^{kz}, \quad W_2(z,s) = B_2(s) e^{-kz}. \tag{20}$$

These homogeneous solutions are subject to matching conditions at the contact ($z = h(x,t) = \eta(t)e^{ikx}$). The number of jump conditions that must be satisfied across an MHD contact discontinuity depends on its type, which has yet to be discussed for the present problem. However, two conditions must be satisfied for every type of contact discontinuity: the normal velocity w and total pressure $p + \mathbf{B} \cdot \mathbf{B}/2$ must be continuous. As only two matching conditions are required to determine the solution in this case, the derivation can proceed without assuming the contact is of a certain type. The first matching condition used is the kinematic condition that w' must be continuous. To leading order in h, this is equivalent to

$$[W]_{z=0} = 0 \to A_1(s) = B_2(s) \equiv A(s), \tag{21}$$

where $[q]_{z=0} \equiv q_2|_{z=0} - q_1|_{z=0}$ and Eq. (20) was used to obtain the expression on the right.

The second matching condition, which accounts for the forcing, is derived by integrating Eq. (9) in z across its inhomogeneous region, which extends from 0 to $h(x,t) \ll 1$ as illustrated in Fig. 3. Along the path indicated, which is contained within fluid 1, Eq. (9) simplifies to

$$\rho_1 \frac{\partial w_1'}{\partial t} + \frac{\partial p_1'}{\partial z} + B\left(\frac{\partial B_{x1}'}{\partial z} - \frac{\partial B_{z1}'}{\partial x}\right) = (\rho_2 - \rho_1)V\delta(t). \tag{22}$$

Integrating Eq. (22) in z from 0 to h yields

$$\rho_1 \int_0^h \frac{\partial w_1'}{\partial t} dz + p_1'(x,h,t) - p_1'(x,0,t) + B\left(B_{x1}'(x,h,t) - B_{x1}'(x,0,t) - \int_0^h \frac{\partial B_{z1}'}{\partial x} dz\right) = (\rho_2 - \rho_1)V\delta(t)h. \tag{23}$$

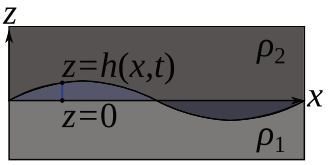

FIG. 3. Inhomogeneous region of the governing equations and integration path used to derive the dynamic condition.

Assuming $\partial w_1'/\partial t$ and $\partial B_{z1}'/\partial x$ are smooth within the inhomogeneous region, the remaining integrals can be approximated by

$$\rho_1 \int_0^h \frac{\partial w_1'}{\partial t} dz \approx \rho_1 h \frac{\partial w_1'}{\partial t}\bigg|_{z=0}, B \int_0^h \frac{\partial B_{z1}'}{\partial x} dz \approx Bh \frac{\partial B_{z1}'}{\partial x}\bigg|_{z=0}. \tag{24}$$

These terms are $O(h^2)$ and thus can be neglected. Next, consider the terms evaluated at the contact discontinuity $z = h$. The continuity of $p + \mathbf{B} \cdot \mathbf{B}/2$ across the contact can be expressed as

$$\left[p' + \frac{1}{2}(B\hat{\mathbf{e}}_x + \mathbf{B}') \cdot (B\hat{\mathbf{e}}_x + \mathbf{B}')\right] = \left[p' + BB_x'\right] + H.O.T. = 0. \tag{25}$$

Thus, to leading order, assuming p_2' and B_{x2}' are smooth

$$p_1'(x, h, t) + BB_{x1}'(x, h, t) = p_2'(x, h, t) + BB_{x2}'(x, h, t) \approx p_2'(x, 0, t) + BB_{x2}'(x, 0, t). \tag{26}$$

Combining Eq. (23) with Eqs. (24) and (26), neglecting products of perturbations and higher order terms in h, yields the final form of the dynamic condition:

$$p_2'(x, 0, t) - p_1'(x, 0, t) + B\left[B_{x2}'(x, 0, t) - B_{x1}'(x, 0, t)\right] = (\rho_2 - \rho_1) V \delta(t) \eta(t) e^{ikx}. \tag{27}$$

D. Oscillatory solutions

Taking the Laplace transform of Eq. (27) then using Eqs. (12)–(17) to express all variables in terms of W_1 and W_2 gives

$$[(\rho_1 + \rho_2)\frac{s}{k} + \frac{2kB^2}{s}]A(s) = (\rho_2 - \rho_1) V \eta_0, \tag{28}$$

where the expressions for W_1 and W_2 given in Eq. (20) have been used. The final solutions for the vertical velocity perturbations are obtained by solving Eq. (28) for $A(s)$, taking the inverse Laplace transform, then substituting the result in the assumed forms of the perturbations. This gives

$$w_1'(x, z, t) = kV\eta_0 \mathcal{A} \cos(\omega t)\, H(t)\, e^{kz} e^{ikx}, \tag{29}$$

$$w_2'(x, z, t) = kV\eta_0 \mathcal{A} \cos(\omega t)\, H(t)\, e^{-kz} e^{ikx}, \tag{30}$$

where

$$\omega = \frac{Bk}{\sqrt{(\rho_1 + \rho_2)/2}} = \frac{k}{\sqrt{\frac{1}{2}\left(c_{A1}^{-2} + c_{A2}^{-2}\right)}}, \mathcal{A} \equiv \frac{\rho_2 - \rho_1}{\rho_2 + \rho_1}.$$

Here, $\mathcal{A}$ is the Atwood ratio and $c_{Aj} = B/\sqrt{\rho_j}$ is the Alfvén speed. This solution shows that while the initial ($t = 0^+$) growth rate of the interface,

$$\frac{\partial \eta}{\partial t}\bigg|_{t=0} = w_j'(0, 0, 0^+) = \eta_0 kV\mathcal{A}, \tag{31}$$

is identical to the hydrodynamic case,[2] the presence of the magnetic field prevents linear growth at this rate. Instead, the amplitude of the interface oscillates in time at a frequency ω, as described by

$$\eta(t) = \eta_0 + \int_{0^+}^t w_j'(0, 0, \tau)\, d\tau = \eta_0 \left(1 + \frac{kV\mathcal{A}}{\omega} \sin(\omega t)\right) = \eta_0 + \Delta\eta \sin(\omega t). \tag{32}$$

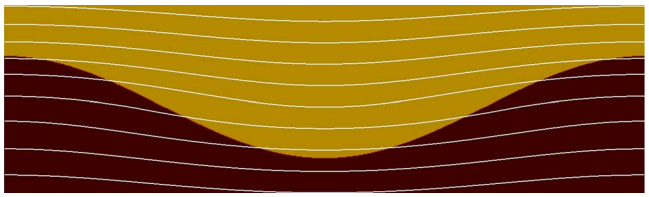

FIG. 4. Density contours overlaid with magnetic field lines at $t = 1/5\omega$ from the linear solution to the incompressible model problem. The case shown is characterised by $\rho_1 = 1.26$, $\rho_2 = 1.57$, $p_0 = 1.47$, $B_{x0} = 0.628$, and $\eta_0 = 0.0395\lambda$.

For one set of parameters, the resulting density field at $t = 1/5\omega$ is shown in Fig. 4 along with the magnetic field lines. It can be seen that the motion of the interface has perturbed the magnetic field lines, which creates a restoring force due to magnetic field line tension. This causes the fluids to oscillate, however, it will be shown in Sec. IV that this does not completely describe the flow physics around the interface.

One aspect of the solution that requires further investigation is the nature of the interface. The unperturbed interface has no magnetic field lines crossing it and is known as a tangential discontinuity. Only the normal velocity w and $p + \mathbf{B} \cdot \mathbf{B}/2$ are required to be continuous across a tangential discontinuity (see, e.g., Sutton and Sherman[25]), and these were the only constraints built into the solution of the model problem. If the field lines cross the interface, however, as is seen to occur in Fig. 4, two additional constraints must be satisfied: continuity of tangential velocity and magnetic field. The tangential velocities on either side of the interface may be computed by substituting the solutions for w_j' given in Eqs. (29) and (30) into Eq. (7). The jump in tangential velocity across the interface is found to be non-zero and is given by

$$[u]_{z=0} = 2V\eta_0 \mathcal{A} \cos(\omega t)\, H(t) \sin(kx). \tag{33}$$

This implies that the inhomogeneous region between the two fluids, which we integrated across in our solution, must contain more structure than a simple MHD contact discontinuity. Additional structures must be present in this matching region to carry the shear. To investigate the nature of these structures, and determine whether our model, in which integration across them is utilized, accurately predicts the motion of the interface, we turn to nonlinear compressible simulations. Note that this issue can be avoided by a slight modification to the initial conditions: if the magnetic field lines have the same initial perturbation as the interface, they will remain parallel to it for all time, permitting the interface to be a tangential discontinuity. While this eliminates the need for additional flow structures, the perturbed field lines will cause oscillation of the interface even in the absence of any forcing, as seen in the model of Cao *et al.*[16]

III. SIMULATION METHODOLOGY

A. Unsplit method for ideal MHD

The nonlinear simulations were carried out using a compressible ideal MHD code similar to that developed by Samtaney[12] and Samtaney *et al.*[26] Key details of the algorithm are presented here for completeness. We write the equations of ideal MHD in conservation form as follows:

$$\frac{\partial U}{\partial t} + \sum_{d=0}^{\mathbf{D}-1} \frac{\partial F_d}{\partial x_d} = 0, \tag{34}$$

where $\mathbf{D}$ is the dimensionality of physical space, $U = \{\rho, \rho u_i, B_i, e\}^T$, e is the total energy per unit volume, and the flux vector is given by

$$F_j(U) = \{\rho u_j,\ \rho u_i u_j + (p + \frac{1}{2} B_k B_k)\delta_{ij} - B_i B_j,\ B_i u_j - B_j u_i,\ (e + p + \frac{1}{2} B_k B_k) u_j - B_j (B_k u_k)\}.$$

Here, we limit our discussion to two dimensions ($\mathbf{D} = 2$).

We define a vector of variables called the "primitive variables" $W(U) = \{\rho\ ,\ u_i, B_i\ ,\ p\ )\}^T$. Rewriting the equations using W in quasilinear form, we get

$$\frac{\partial W}{\partial t} + \sum_{d=0}^{\mathbf{D}-1} A_d(W)\frac{\partial W}{\partial x_d} = 0, \quad A^d = \nabla_U W \cdot \nabla_U F^d \cdot \nabla_W U, \tag{35}$$

A^d is a singular matrix with an eigenvector degeneracy. The unsplit algorithm is essentially a predictor-corrector method in which face-centered and time-centered primitive variables are predicted, followed by a corrector step in which a Riemann problem is solved using the predicted values to compute a second order accurate estimate of the fluxes: $F^{n+\frac{1}{2}}_{\boldsymbol{i}+\frac{1}{2}\boldsymbol{e}^d} \approx F^d(\boldsymbol{x}_0 + (\boldsymbol{i} + \frac{1}{2}\boldsymbol{e}^d)h, t^n + \frac{1}{2}\Delta t)$, where $\boldsymbol{x}_0$ is the position of the lower left corner of the domain, $\boldsymbol{i}$ is a $\mathbf{D}$-tuple index, $\boldsymbol{e}^d$ is the unit vector in the d-direction, h is the grid spacing and Δt is the discrete time step. The predictor step is further divided into a normal and a transverse predictor steps. We fit linear profiles in each computational cell, and compute slopes $\Delta^d W_{\boldsymbol{i}}$ which are subsequently limited in characteristic space using Van Leer slope limiting. The normal predictor consists of the effect of the normal derivative terms on the extrapolation in space and time from cell centers to faces. In this step, we split the primitive variables as follows

$$W^n_{\boldsymbol{i}} = \begin{pmatrix} \bar{W}^n_{\boldsymbol{i}} \\ B^n_{\boldsymbol{i},d} \end{pmatrix}. \tag{36}$$

For $0 \le d < \mathbf{D}$,

$$\bar{W}_{\boldsymbol{i},\pm,d} = \bar{W}^n_{\boldsymbol{i}} + \frac{1}{2}(\pm I - \frac{\Delta t}{h}\bar{A}^d_{\boldsymbol{i}})P_{\pm}(\Delta^d W_{\boldsymbol{i}}), \tag{37}$$

$$\bar{A}^d_{\boldsymbol{i}} = \bar{A}^d(W_{\boldsymbol{i}}), \quad P_{\pm}(W) = \sum_{\pm\lambda_k > 0} (l_k \cdot W) r_k,$$

$$B_{\boldsymbol{i},\pm,d} = B_{\boldsymbol{i},d}, \quad W^n_{\boldsymbol{i},\pm,d} = \begin{pmatrix} \bar{W}^n_{\boldsymbol{i},\pm,d} \\ B^n_{\boldsymbol{i},\pm,d} \end{pmatrix},$$

where $\bar{A}^d_{\boldsymbol{i}}$ is the matrix obtained from $A^d_{\boldsymbol{i}}$ after deleting the row and column corresponding to the normal component of the magnetic field, λ_k are eigenvalues of $\bar{A}^d_{\boldsymbol{i}}$, and l_k and r_k are the corresponding left and right eigenvectors. This step is followed by the so-called "Stone Correction" to the above normal predicted states.[26] This stems from the fact that in multi-dimensions the derivative of the normal component of the magnetic field in the d-direction is not zero. The Stone Correction is given as

$$\bar{W}_{\boldsymbol{i},\pm,d} = \bar{W}_{\boldsymbol{i},\pm,d} - \frac{\Delta t}{2}\left(\frac{\partial B_d}{\partial x_d}\right)_{\boldsymbol{i}} a_B, \tag{38}$$

where $a_B = \left\{0, B_k/\rho, u_{d_1}, u_{d_2}, -(\gamma - 1)u_k B_k\right\}^T$, and $d_l = mod(d + l, 3)$; and the term $(\frac{\partial B_d}{\partial x_d})_{\boldsymbol{i}}$ is the derivative of the normal component of the magnetic field in the d-direction, computed using a standard second-order central difference formula. The above normal predictor step gives us left and right states at each cell interface. A correction stemming from the transverse derivatives to the fluxes is required in addition to the normal predictor step. For this transverse predictor step, we compute estimates of F^d suitable for computing 1D flux derivatives $\frac{\partial F^d}{\partial x^d}$ using a Riemann solver. We employ a seven-wave linearized Riemann solver (see, e.g., Ryu and Jones[24]) to obtain the primitive variables at the cell faces, except the normal component of the magnetic field, which is taken as the arithmetic mean of the left and right states. The entire solution vector at $\boldsymbol{i} + \frac{1}{2}\boldsymbol{e}^d$ is termed as the solution of the Riemann problem $R(.\ ,.)$. The fluxes are then computed from the primitive variables as

$$F^{1D}_{\boldsymbol{i}+\frac{1}{2}\boldsymbol{e}^d} \equiv F^{1D}(W_{\boldsymbol{i}+\frac{1}{2}\boldsymbol{e}^d}), \quad W_{\boldsymbol{i}+\frac{1}{2}\boldsymbol{e}^d} \equiv R(W_{\boldsymbol{i},+,d}, W_{\boldsymbol{i}+\boldsymbol{e}^d,-,d}). \tag{39}$$

Final corrections are then made to $W_{\boldsymbol{i},\pm,d}$ due to the transverse derivatives:

$$W^{n+\frac{1}{2}}_{\boldsymbol{i},\pm,d} = W_{\boldsymbol{i},\pm,d} - \frac{\Delta t}{2h}\nabla_U W \cdot (F^{1D}_{\boldsymbol{i}+\frac{1}{2}\boldsymbol{e}^{d_1}} - F^{1D}_{\boldsymbol{i}-\frac{1}{2}\boldsymbol{e}^{d_1}}) \quad d \neq d_1,\ 0 \leq d, d_1 < \mathbf{D}. \tag{40}$$

To obtain a final estimate of the fluxes, we first compute the solution to the Riemann problem using the time-centered predicted states,

$$W^{n+\frac{1}{2}}_{\boldsymbol{i}+\frac{1}{2}\boldsymbol{e}^d} = R(W^{n+\frac{1}{2}}_{\boldsymbol{i},+,d}, W^{n+\frac{1}{2}}_{\boldsymbol{i}+\boldsymbol{e}^d,-,d}, d). \tag{41}$$

Then, using the normal component of the magnetic field at cell faces $\boldsymbol{i} + \frac{1}{2}\boldsymbol{e}^d$, compute a cell centered divergence. To eliminate this divergence, the following Poisson equation is solved using a multigrid technique with a Gauss-Seidel Red-Black ordering smoother,

$$\nabla^2\chi = \sum_{d=0}^{\mathbf{D}-1} \frac{\partial B_d}{\partial x_d}_{\boldsymbol{i}}. \tag{42}$$

The magnetic field is then corrected to be $B_{\boldsymbol{i}+\frac{1}{2}\boldsymbol{e}^d} = B_{\boldsymbol{i}+\frac{1}{2}\boldsymbol{e}^d} - \nabla\chi$, and substituted into $W^{n+\frac{1}{2}}_{\boldsymbol{i}+\frac{1}{2}\boldsymbol{e}^d}$, which is used to compute the final fluxes $F^{n+\frac{1}{2}}_{\boldsymbol{i}+\frac{1}{2}\boldsymbol{e}^d} = F(W^{n+\frac{1}{2}}_{\boldsymbol{i}+\frac{1}{2}\boldsymbol{e}^d})$. These fluxes are used to finally update the conserved variables via

$$U^{n+1}_{\boldsymbol{i}} = U^n_{\boldsymbol{i}} - \frac{\Delta t}{h}\sum_{d=0}^{\mathbf{D}-1}(F^{n+\frac{1}{2}}_{\boldsymbol{i}+\frac{1}{2}\boldsymbol{e}^d} - F^{n+\frac{1}{2}}_{\boldsymbol{i}-\frac{1}{2}\boldsymbol{e}^d}). \tag{43}$$

B. Simulation details and grid convergence

The geometry for the nonlinear simulations is as shown in Fig. 2. Periodic boundary conditions are used in the x-direction and zero gradient boundary conditions are used in the z-direction. In all simulations, the ratio of specific heats is set to $\gamma = 5/3$ and the state upstream of the shock is used to non-dimensionalize the equations, thus the initial density below the interface is $\rho_1 = 1$ and the pressure upstream of the shock is $p_0 = 1$. For the reference shock-driven simulation, the initial density above the interface is $\rho_2 = 5/4$ and the shock has a sonic Mach number $M = 1.1$. The initial perturbation amplitude of the interface is $\eta_0/\lambda = 1/50$ and the uniform horizontal magnetic field upstream of the shock is characterised by $\beta = 2p_0/B^2_{x0} = 16$ ($B_{z0} = 0$ for all simulations). The conditions downstream of the shock are obtained from the MHD Rankine-Hugoniot relations. As the magnetic field is perpendicular to the shock normal, the driving shock is what is known as a perpendicular shock. Perpendicular shocks are always fast as in their direction of propagation only the fast characteristic speed is non-zero and is given by $c_f = (c_A^2 + a^2)^{1/2}$. The shock-interaction process compresses the fluids to higher densities and pressure, increases the magnetic field strength and compresses the interface perturbation. Post-shock-compression values are used to evaluate the behavior of the current model. For the reference case, these are $\rho_1 = 1.10$, $\rho_2 = 1.37$, $p_0 = 1.16$, $B_{x0} = 0.387$, and $\eta_0 = 0.0179\lambda$. The magnitude of the impulse is set to the velocity imparted to the interface in the shock driven problem: $V = 0.111$. Shock driven simulations of other cases are setup in the same manner as the reference case, but with altered ρ_2, M, η_0/λ, or β. The corresponding model evaluations make use of the resulting post-shock-compression parameters.

A uniform grid spacing of $\Delta x = \lambda/250$ is utilized for all simulations used to characterise interface behavior. To evaluate the adequacy of this resolution, the reference simulation was repeated with grid spacings of $\Delta x = \lambda/500$ (medium grid) and $\Delta x = \lambda/1024$ (fine grid). The normalized interface amplitude histories from these simulations are shown in Fig. 5(a). The amplitude ($\Delta\eta$) and frequency (ω) of the interface oscillations in these histories are estimated using nonlinear least-squares fitting of the first two periods of data to a function of the form $\eta_0 + \Delta\eta\sin[\omega(t - t_0)]$. The convergence of these two key statistics is examined using generalized Richardson extrapolation for unequal

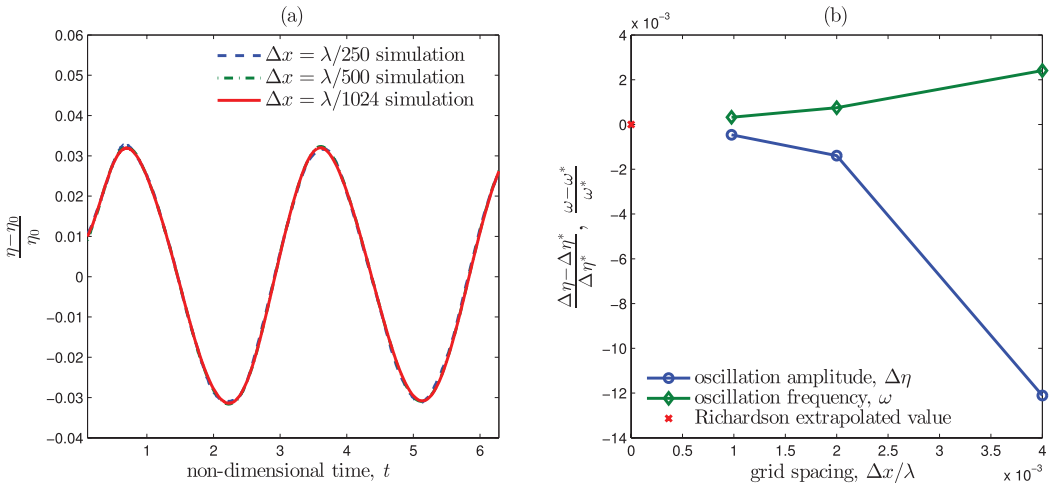

FIG. 5. (a) Interface amplitude histories from the shock-driven simulations of a case characterised by $M = 1.1$, $\rho_2/\rho_1 = 5/4$, $\beta = 16$, and $\eta_0 = \lambda/50$ at different resolutions ($\Delta x/\lambda$). (b) Convergence of interface statistics to Richardson extrapolated values.

refinement ratios, as detailed in Stern *et al.*[27] The orders of convergence of $\Delta\eta$ and ω are estimated to be 1.54 and 1.18, respectively. The convergence of these statistics to their Richardson extrapolated values for $\Delta x \to 0$ (denoted with a superscript *) is shown in Fig. 5(b). For the simulation on the coarse grid, $\Delta\eta$ and ω differ from their Richardson extrapolated values by -1.21% and 0.241%, respectively. This demonstrates that the effect of discretization error on the behavior of the interface, which is of primary interest here, is acceptably small. In ideal MHD simulations, there is no physical dissipation to set a minimum length scale, thus point-wise convergence of the solution with grid refinement cannot be expected. As the grid is refined, numerical diffusion decreases, which, for example, causes all discontinuities to be more sharply resolved. In order to more clearly illustrate the wave structures in the vicinity of the interface, results fine-grid ($\Delta x = \lambda/1024$) simulations are used to generate contour plots.

IV. RESULTS

A. The reference case

For the reference case ($M = 1.1$, $\beta = 16$, $\rho_2/\rho_1 = 5/4$, and $\eta_0 = \lambda/50$), the evolution of vorticity in the vicinity of the interface from the shock-driven simulation is shown in Fig. 6. The baroclinic generation of vorticity during the shock-interface interaction is not affected by the magnetic field. The first frame of Fig. 6 shows the vorticity field immediately following the completion of the shock interaction. It shows that only a small fraction of the vorticity is transported by the transmitted and reflected fast shocks while the majority lies on the contact discontinuity, in good agreement with the linear model at $t = 0^+$. If the vorticity remained on the contact, as in the hydrodynamic case, its induced velocity would cause the perturbation of the interface to grow and eventually roll-up of the interface would occur. This cannot occur physically, however, as the MHD Rankine-Hugoniot relations prohibit steady shear across a contact discontinuity that is penetrated by magnetic field lines. Instead, the initial vorticity (and current) distribution is seen to break up into two vorticity-carrying waves that propagate parallel and anti-parallel to the magnetic field. In the incompressible limit, these waves are discontinuous, finite amplitude shear Alfvén waves. At each point, their phase speed is equal to the local Alfvén speed. The corresponding waves in the compressible simulation are closely approximated by incompressible waves as only small perturbations in density occur through them. In Fig. 6, it can be seen that the structure of these waves remains unchanged as they interact with each other. At $t = T/2$, where $T = 2\pi/\omega$ is the theoretical period from the linear model, the waves constructively interfere to form a vorticity distribution π radians out-of-phase with the

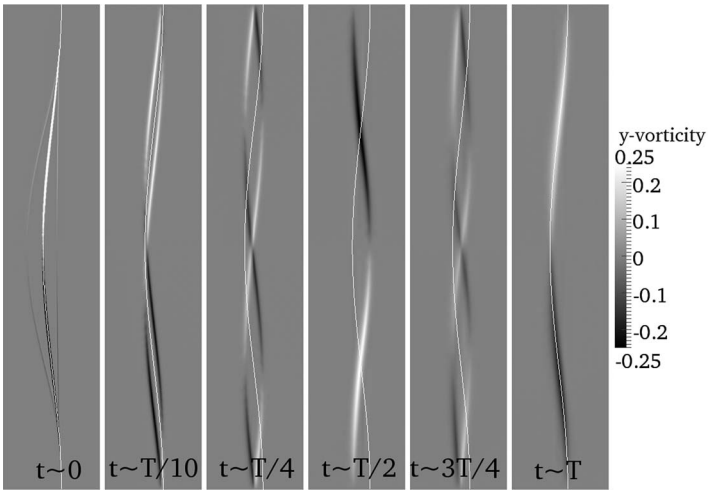

FIG. 6. Evolution of vorticity in the vicinity of the interface from the shock-driven simulation of the reference case ($M = 1.1$, $\rho_2/\rho_1 = 5/4$, $\beta = 16$, and $\eta_0 = \lambda/50$). The position of the interface is indicated by a single white density contour corresponding to $\rho = (\rho_1 + \rho_2)/2$. Note that the domain has been rotated clockwise by $\pi/2$ radians to make the figure more compact.

original. This will reverse the growth of the interface perturbation caused by the vorticity distribution at $t = 0^+$. The periodic constructive interference (with alternating phase) of the waves continues with time and causes the interface to oscillate, as predicted by the linear model.

The nonlinear simulation has established that waves do exist in the vicinity of the interface to support shear across the matching region while allowing the contact discontinuity to satisfy the relevant jump conditions. We now investigate whether the linear model, which was derived by integrating across this region, can accurately predict the behavior of the interface. This is assessed in Fig. 7, which shows the interface amplitude histories from the incompressible model and the shock-driven compressible simulation. The model accurately predicts the oscillatory nature of the interface motion, with the frequency ω being predicted to within 1.6%. This difference is significantly greater than the estimated numerical error in ω of 0.24%, thus the agreement is unlikely to be fortuitous. The same statement holds for all model-to-simulation frequency comparisons made in Secs. IV B–IV E. The wave structure observed in the compressible simulation indicates that the path-length of each wave is evenly split between the two fluids. Thus the period of the waves, and consequently the interface oscillation, can be estimated by

$$T_{wave} = \frac{\lambda/2}{c_{A1}} + \frac{\lambda/2}{c_{A2}} = \frac{\lambda}{2B}\left(\sqrt{\rho_1} + \sqrt{\rho_2}\right),$$

assuming the waves travel at the Alfvén speed in each fluid and are solitary. The ratio between the corresponding oscillation frequency and that predicted by the incompressible model is given by

$$\frac{\omega_{wave}}{\omega_{model}} = \frac{\sqrt{\frac{1}{2}(\rho_1 + \rho_2)}}{\frac{1}{2}\left(\sqrt{\rho_1} + \sqrt{\rho_2}\right)}.$$

For the reference conditions, this ratio is approximately 1.002, which explains the accurate prediction of the simulated oscillation frequency. The amplitude of the oscillations, $\Delta\eta$, in the simulation is over-predicted by the model of an average of 12.6% over the first two periods. The numerical error in $\Delta\eta$ from the simulation, estimated to be -1.2%, makes a relatively minor contribution to this over-prediction. For all cases examined in Secs. IV B–IV E, the estimated numerical error in $\Delta\eta$ is also small compared to the difference between model and simulation. Figure 7 shows that for the reference case, the agreement is initially closer than 12.6%, but as numerical dissipation damps the oscillation of the interface in the simulation, the discrepancy in $\Delta\eta$ increases. Two factors that contribute to the model over-predicting $\Delta\eta$ can be readily identified: First, the model does

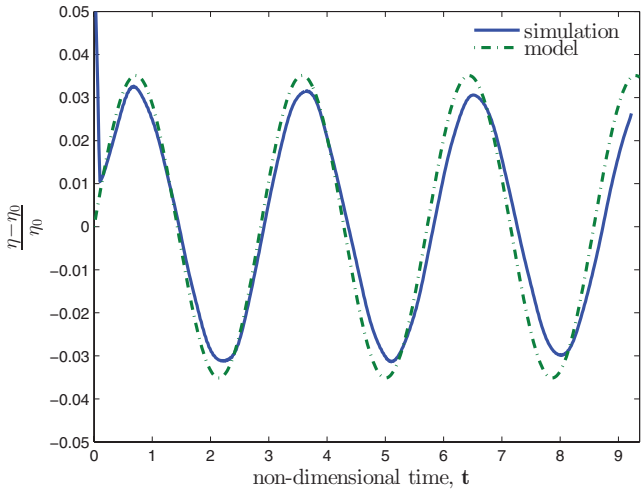

FIG. 7. Interface amplitude histories from the shock-driven simulation and the linear model of the reference case. The shock-driven case is characterised by $M = 1.1$, $\rho_2/\rho_1 = 5/4$, $\beta = 16$, and $\eta_0 = \lambda/50$.

not account for the small fraction of vorticity that is rapidly transported from the interface by the transmitted and reflected fast shocks. Second, the model treats all vorticity as being present at $z = 0$ and takes $w'(x, 0, t)$ to be the interfacial growth rate, effectively neglecting the amplitude of the interface and waves in z as these are second-order effects. For finite perturbation amplitudes, such as the 2% used in the reference case, this vertical displacement reduces the induced velocities at the interface extrema and thus $\Delta\eta$.

B. Effect of increasing shock strength

To assess the effects of increasing shock strength on the MHD RMI, simulations have been carried out for incident shock sonic Mach numbers of $M = 1.25$ and $M = 2$, with the remaining parameters fixed to their values in the reference case. The interface amplitude histories from these simulations are compared to the $M = 1.1$ reference case and predictions from the model in Fig. 8. As shock strength increases, both the frequency and amplitude of the interface oscillations increase

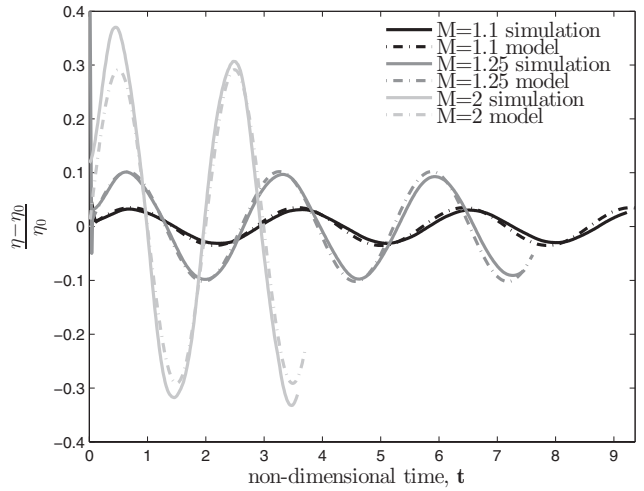

FIG. 8. Interface amplitude histories from the shock-driven simulations and the linear model for $\rho_2/\rho_1 = 5/4$, $\beta = 16$, $\eta_0 = \lambda/50$, and various M.

and appear to scale as predicted by the model. Greater shock compression at higher Mach numbers causes both ρ and B at the interface to increase with M. As the oscillation frequency scales with $B/\sqrt{\rho}$, this results in a sub-linear increase in ω with M. The accuracy of the frequency predicted by the model appears insensitive to M: the relative difference from ω extracted from the corresponding simulation is 1.6% at $M = 1.1$, 1.4% at $M = 1.25$, and -1.5% at $M = 2$.

The growth in $\Delta\eta$ with M is a result of the increasing velocity V imparted to the interface. This overwhelms the damping effect of the increase in $\omega \propto B/\sqrt{\rho}$. The model predicts $\Delta\eta$ reasonably at all M simulated: the relative difference is 12.6% at $M = 1.1$, 4.4% at $M = 1.25$, and -10.3% at $M = 2$. Figure 8 reveals a large initial spike in η for $M = 2$ that is not captured by the model. This is likely due to the growth caused by the vorticity transported by the transmitted and reflected fast shocks, which is only significant at early times when these shocks are close to the interface.

C. Effect of increasing magnetic field

To assess the effects of increasing magnetic field strength on the MHD RMI, simulations have been carried out for $\beta = 4$ and $\beta = 1$, with the remaining parameters except M fixed to their values in the reference case. In order for the incident shock to exist for all β investigated, $M = 2$ was used. The interface amplitude histories from the $\beta = 16$ and $\beta = 1$ simulations are compared to predictions from the model in Fig. 9. It can be seen that, as predicted by the model, increasing magnetic field strength restricts $\Delta\eta$ and increases ω. There are two primary causes of these effects: the vorticity carrying waves in the vicinity of the interface propagate faster, causing more rapid but smaller amplitude oscillations; and the compression of the shock decreases, resulting in lower baroclinic vorticity production. The lowering of shock compression with increasing β results in the velocity imparted to the interface by the shock interaction dropping from $V = 1.33$ at $\beta = 16$ to $V = 1.21$ and $V = 0.779$ at $\beta = 4$ and $\beta = 1$, respectively.

Figure 9 indicates that for $\beta = 1$, the interface deviates from sinusoidal oscillation at early times. This can be understood by examining how the distribution of vorticity at early times changes with β, which is illustrated in Fig. 10. For $\beta = 16$, the majority of vorticity lies on the interface at early times, while for $\beta = 1$ a much greater fraction is transported by the transmitted and reflected fast shocks. The vorticity on the fast shocks has constant phase with respect to the interface. Thus, it causes growth of the interface rather than oscillation, with the growth rate decaying as the shocks propagate away from the interface. For $\beta = 16$, the vorticity on the fast shocks is weak enough that it induces only a perturbation on the oscillatory behavior of the interface. For $\beta = 1$, however, it is strong enough to cause a significant departure from sinusoidal oscillation for the first two nominal

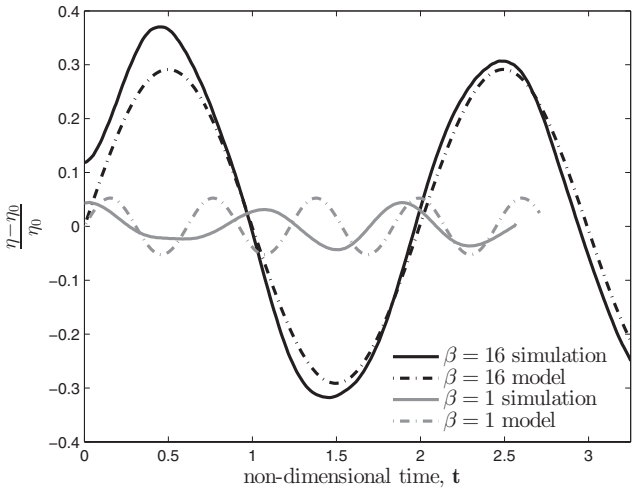

FIG. 9. Interface amplitude histories from the shock-driven simulations and the linear model for $M = 2$, $\rho_2/\rho_1 = 5/4$, $\eta_0 = \lambda/50$, and various β.

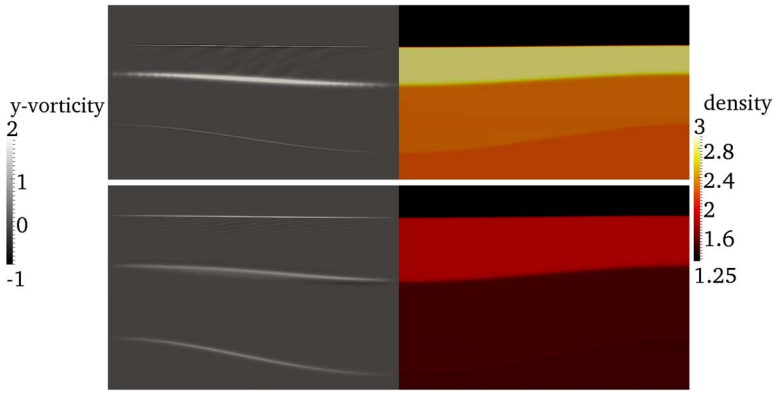

FIG. 10. Post shock-interaction vorticity (left half frames) and density (right half frames) fields for $M = 2$, $\rho_2/\rho_1 = 5/4$, $\eta_0 = \lambda/50$, $\beta = 16$ (top), and $\beta = 1$ (bottom).

periods. This non-sinusoidal behavior, coupled with the removal of vorticity from the vicinity of the interface (in the model, all vorticity remains there), naturally causes the incompressible model to be inaccurate for strong magnetic fields. The relative difference in $\Delta\eta$ increases from -10.25% at $\beta = 16$ to -38.6% at $\beta = 4$ and finally 48.6% at $\beta = 1$.

D. Effect of increased perturbation amplitude

The incompressible model predicts $\eta(t)/\eta_0$ is independent of η_0. To investigate how valid this is in the nonlinear compressible case, additional simulations were carried out for $\eta_0/\lambda = 1/100$ and $\eta_0/\lambda = 1/10$. Values from the reference case were used for the other parameters. The normalized η histories from these simulations are compared to that from the reference case and the model prediction in Fig. 11. The oscillation frequencies from all three simulations are in good agreement with the model, with the maximum difference being 1.9%. For the lower η_0 simulations, $\Delta\eta$ is also reasonably predicted by the model with differences of 10.9% and 12.6% for $\eta_0/\lambda = 1/100$ and $\eta_0/\lambda = 1/50$, respectively. For $\eta_0/\lambda = 1/10$, however, $\Delta\eta/\eta_0$ is substantially lower, resulting in the model over-predicting it by 69.6%. This discrepancy is due, in part, to the model approximating all vorticity

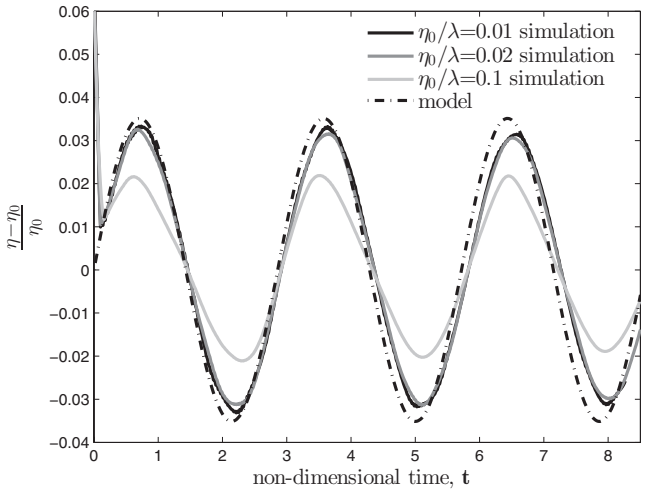

FIG. 11. Interface amplitude histories from the shock-driven simulations and the linear model for $M = 1.1$, $\beta = 16$, $\rho_2/\rho_1 = 5/4$, $\eta_0 = \lambda/50$, and various η_0.

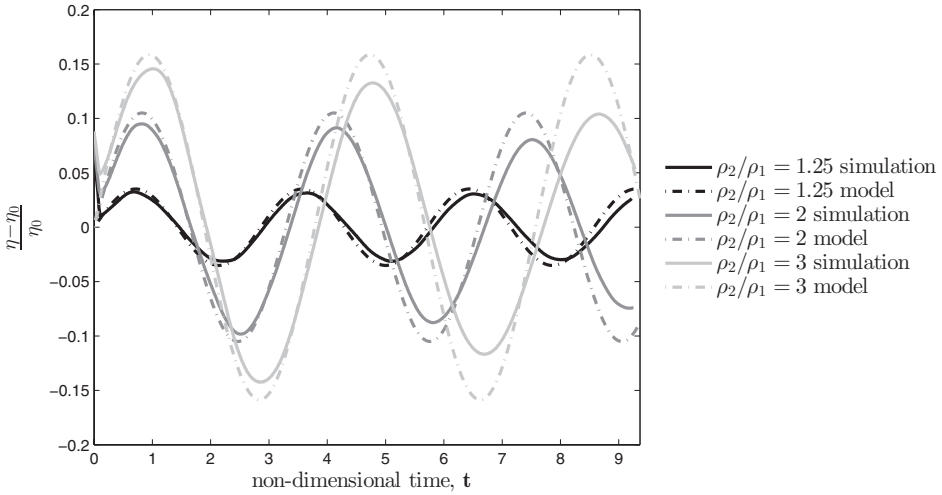

FIG. 12. Interface amplitude histories from the shock-driven simulations and the linear model for $M = 1.1$, $\beta = 16$, $\eta_0 = \lambda/50$, and various ρ_2/ρ_1.

as being present at $z = 0$ and taking $w'(x, 0, t)$ at to be the growth rate of η. For larger η_0, the vertical extent of the interface and the waves substantially decreases the growth rate of η.

E. Effect of increasing Atwood number

The effect of fluid densities on the MHD RMI was investigated for density ratios (ρ_2/ρ_1) of 5/4, 2, and 3, corresponding to Atwood numbers ($\mathcal{A}$) of 1/9, 1/3, and 1/2, respectively. The normalized η histories from the relevant simulations are shown in Fig. 12, along with the incompressible model predictions. As ρ_2 is increased, the Alfvén speed in the heavy fluid decreases like $\rho_2^{-1/2}$, which causes the observed decrease in ω. This decrease is accurately predicted by the model, with the maximum discrepancy in ω for all three simulations being 1.8%.

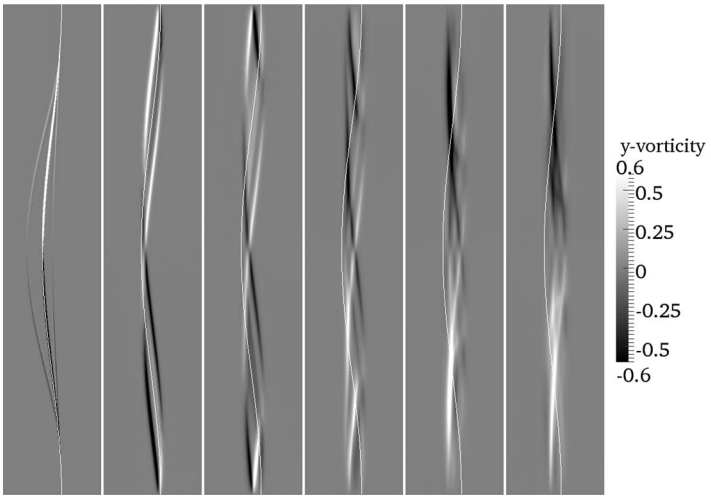

FIG. 13. Evolution of vorticity in the vicinity of the interface from the MHD RMI simulation with $M = 1.1$, $\rho_2/\rho_1 = 3$ ($\mathcal{A} = 1/2$), $\beta = 16$, and $\eta_0 = \lambda/50$). Frames are equispaced in time and span approximately half an oscillation period. The position of the interface is indicated by a single white density contour corresponding to $\rho = (\rho_1 + \rho_2)/2$. Note that the domain has been rotated clockwise by *pi*/2 radians to make the figure more compact.

Figure 12 shows that $\Delta\eta$ increases rapidly with $\mathcal{A}$. This is due to a combination of the linear dependence of the interfacial growth rate on $\mathcal{A}$ and the decrease in ω, to which the growth rate is inversely proportional in the model. For the first oscillation period, the model predicts $\Delta\eta$ with similar accuracy for all $\mathcal{A}$ considered. For higher $\mathcal{A}$, however, the interface oscillations become more rapidly dissipated. To investigate the cause of this, the evolution of the wave structure near the interface for $\mathcal{A} = 1/2$ is plotted in Fig. 13. As the vorticity carrying waves traverse the interface in the x-direction, they appear to produce transmitted and reflected waves. This continuously increases the complexity of the wave structure. It is likely that this process also occurs at lower $\mathcal{A}$, but that the additional waves generated are too weak to appear in the visualizations presented. In the final frame of Fig. 13, after approximately half an oscillation period, the system of waves has coalesced to resemble the original vorticity distribution, but π radians out-of-phase. Thus, the more complex system of waves is still capable of producing oscillatory behavior. However, the fine scale wave structure present in this case will be more rapidly diffused by numerical dissipation, which causes $\Delta\eta$ to decay with time.

V. CONCLUSIONS

We have investigated the MHD Richtmyer-Meshkov instability for the case where the initial magnetic field is unperturbed and aligned with the mean interface location. This differs from the situation modeled by Cao *et al.*,[16] who assumed the magnetic field lines have the same initial perturbation as the interface. In both cases, the impulsive acceleration results in the interface perturbation amplitude oscillating with time, but the small change in the initial conditions greatly alters the flow physics at the interface and hence the mechanism by which the instability is suppressed. In the work of Cao *et al.*,[16] the interface is permitted to be a vortex sheet and the instability is suppressed by magnetic field line tension. In the case investigated here, the vorticity distribution present on the interface immediately after the shock interaction breaks up into waves traveling parallel and anti-parallel to the magnetic field, which transport the vorticity. The interference of these waves, with alternating phase, as they propagate causes the perturbation amplitude of the interface to oscillate in time. This interface behavior is accurately predicted over a broad range of parameters by the incompressible linear model we have developed, which integrates across these waves and the interface. Owing to our use of an equilibrium initial condition, the predicted dynamics are driven only by the impulsive acceleration.

We have carried out nonlinear compressible simulations to investigate the behavior of the transverse field MHD RMI, and the performance of the incompressible model, over a range of shock strengths, magnetic field strengths, perturbation amplitudes, and Atwood numbers. The performance of the model was found to be reasonably insensitive to shock strength, accurately predicting the increase in oscillation frequency and amplitude with Mach number. When the strength of the magnetic field was increased, the interface oscillations followed the trend of increasing frequency and decreasing amplitude predicted by the model. However, the fraction of vorticity carried by transmitted and reflected fast shocks increased with field strength, causing the interface behavior to deviate from sinusoidal oscillation at early times, which resulted in the model being quantitatively inaccurate. For increasing initial perturbation amplitude, the increase in oscillation amplitude was below the linear scaling predicted by the model, but the oscillation frequency was accurately predicted for all amplitudes investigated. Finally, we found that the decrease in frequency and increase in amplitude of interface oscillations with increasing Atwood number were well predicted by the model at early times. In the simulations, however, the oscillations became more rapidly dissipated with time as the Atwood number was increased. The wave structure in the vicinity of the interface was found to become more complex with time.

ACKNOWLEDGMENTS

Dr. Wheatley is the recipient of an Australian Research Council Discovery Early Career Researcher Award (Project No. DE120102942). Additionally, this research was supported under

Australian Research Council's Discovery Projects funding scheme (Project No. DP120102378). Professor Samtaney is partially supported by a KAUST Base Research Award.

[1] G. H. Markstein, "Flow disturbances induced near a slightly wavy contact surface, or flame front, traversed by a shock wave," J. Aeronaut. Sci. **24**, 238 (1957).
[2] R. D. Richtmyer, "Taylor instability in shock acceleration of compressible fluids," Commun. Pure Appl. Math. **13**, 297 (1960).
[3] E. E. Meshkov, "Instability of the interface of two gases accelerated by a shock wave," Fluid Dyn. **4**, 101 (1969).
[4] M. Brouillette, "The Richtmyer-Meshkov instability," Annu. Rev. Fluid Mech. **34**, 445 (2002).
[5] J. D. Lindl, P. Amendt, R. L. Berger, S. G. Glendinning, S. H. Glenzer, S. W. Haan, R. L. Kauffman, O. L. Landen, and L. J. Suter, "The physics basis for ignition using indirect-drive targets on the National Ignition Facility," Phys. Plasmas **11**, 339 (2004).
[6] J. D. Lindl, R. L. McCrory, and E. M. Campbell, "Progress toward ignition and burn propagation in inertial confinement fusion," Phys. Today **45**, 32 (1992).
[7] D. Arnett, "The role of mixing in astrophysics," Astrophys. J., Suppl. Ser. **127**, 213 (2000).
[8] J. Yang, T. Kubota, and E. E. Zukoski, "Applications of shock induced mixing to supersonic combustion," AIAA J. **31**, 854 (1993).
[9] A. M. Khokhlov, E. S. Oran, and G. O. Thomas, "Numerical simulation of deflagration to- detonation transition: the role of shock-flame interactions in turbulent flames," Combust. Flame **117**, 323 (1999).
[10] R. J. Stalker and K. C. A. Crane, "Driver gas contamination in a high-enthalpy reflected shock-tunnel," AIAA J. **16**, 277 (1978).
[11] S. Chandrasekhar, *Hydrodynamic and Hydromagnetic Stability* (Oxford University Press, 1961).
[12] R. Samtaney, "Suppression of the Richtmyer-Meshkov instability in the presence of a magnetic field," Phys. Fluids **15**, L53 (2003).
[13] V. Wheatley, D. I. Pullin, and R. Samtaney, "Regular shock refraction at an oblique planar density interface in manetohydrodynamics," J. Fluid Mech. **522**, 179 (2005).
[14] V. Wheatley, R. Samtaney, and D. I. Pullin, "Stability of an impulsively accelerated perturbed density interface in incompressible MHD," Phys. Rev. Lett. **95**, 125002 (2005).
[15] V. Wheatley, R. Samtaney, and D. I. Pullin, "The Richtmyer-Meshkov instability in magnetohydrodynamics," Phys. Fluids **21**, 082102 (2009).
[16] J. T. Cao, Z. W. Wu, H. J. Ren, and D. Li, "Effects of shear flow and transverse magnetic field on Richtmyer-Meshkov instability," Phys. Plasmas **15**, 042102 (2008).
[17] T. Sano, K. Nishihara, C. Matsuoka, and T. Inoue, "Magnetic field amplification associated with the Richtmyer-Meshkov instability," Astrophys. J. **758**, 126 (2012).
[18] N. E. Lanier, C. W. Barnes, S. H. Batha, R. D. Day, G. R. Magelssen, J. M. Scott, A. M. Dunne, K. W. Parker, and S. D. Rothman, "Multimode seeded Richtmyer-Meshkov mixing in a convergent, compressible, miscible plasma system," Phys. Plasmas **10**, 1816 (2003).
[19] S. H. R. Hosseini and K. Takayama, "Experimental study of Richtmyer-Meshkov instability induced by cylindrical shock waves," Phys. Fluids **17**, 084101 (2005).
[20] K. O. Mikaelian, "Rayleigh-Taylor and Richtmyer-Meshkov instabilities and mixing in stratified cylindrical shells," Phys. Fluids **17**, 094105 (2005).
[21] M. Lombardini and D. I. Pullin, "Small-amplitude perturbations in the three-dimensional cylindrical Richtmyer-Meshkov instability," Phys. Fluids **21**, 114103 (2009).
[22] S. H. Glenzer, B. J. MacGowan, P. Michel, N. B. Meezan, L. J. Suter, S. N. Dixit, J. L. Kline, G. A. Kyrala, D. K. Bradley, D. A. Callahan, E. L. Dewald, L. Divol, E. Dzenitis, M. J. Edwards, A. V. Hamza, C. A. Haynam, D. E. Hinkel, D. H. Kalantar, J. D. Kilkenny, O. L. Landen, J. D. Lindl, S. LePape, J. D. Moody, A. Nikroo, T. Parham, M. B. Schneider, R. P. J. Town, P. Wegner, K. Widmann, P. Whitman, B. K. F. Young, B. Van Wonterghem, L. J. Atherton, and E. I. Moses, "Symmetric inertial confinement fusion implosions at ultra-high laser energies," Science **327**, 1228 (2010).
[23] M. Hohenberger, P.-Y. Chang, G. Fiskel, J. P. Knauer, R. Betti, F. J. Marshall, D. D. Meyerhofer, F. H. Séguin, and R. D. Petrasso, "Inertial confinement fusion implosions with imposed magnetic field compression using the OMEGA Laser," Phys. Plasmas **19**, 056306 (2012).
[24] D. Ryu and T. W. Jones, "Numerical magnetohydrodynamics in astrophysics: algorithm and tests for one-dimensional flow," Astrophys. J. **442**, 228 (1995).
[25] G. W. Sutton and A. Sherman, *Engineering Magnetohydrodynamics* (McGraw-Hill, 1965).
[26] R. Samtaney, P. Colella, T. J. Ligocki, D. F. Martin, and S. C. Jardin, "An adaptive mesh semi-implicit conservative unsplit method for resistive MHD," J. Phys.: Conf. Ser. **16**, 40 (2005).
[27] F. Stern, R. V. Wilson, H. W. Coleman, and E. G. Paterson, "Comprehensive approach to verification and validation of CFD simulations—Part 1: Methodology and procedures," J. Fluids Eng. **123**, 793 (2001).